

PAPER

Electrical characterization of n-doped SiGeSn diodes with high Sn content

To cite this article: Caterina J Clausen *et al* 2018 *Semicond. Sci. Technol.* **33** 124017

View the [article online](#) for updates and enhancements.





IOP | ebooks™

Bringing you innovative digital publishing with leading voices to create your essential collection of books in STEM research.

Start exploring the **collection** - download the first chapter of every title for free.

Electrical characterization of n-doped SiGeSn diodes with high Sn content

Caterina J Clausen¹ , Inga A Fischer¹, David Weisshaupt¹,
Florian Baerwolf² , Bernd Tillack², Gerard Colston³, Maksym Myronov³,
Michael Oehme¹ and Joerg Schulze¹

¹ Institut für Halbleitertechnik (IHT), Universität Stuttgart, Stuttgart, Germany

² IHP, Im Technologiepark 25, Frankfurt (Oder), Germany

³ Department of Physics, The University of Warwick, Coventry, United Kingdom

E-mail: caterina.clausen@iht.uni-stuttgart.de

Received 30 June 2018, revised 3 September 2018

Accepted for publication 24 September 2018

Published 15 November 2018



Abstract

Diodes incorporating undoped and Sb-doped $\text{Si}_x\text{Ge}_{1-x-y}\text{Sn}_y$ layers grown by molecular beam epitaxy with different alloy compositions and lattice-matched to Ge were fabricated and characterized experimentally. We discuss material as well as electrical device characterization and investigate different contact metallizations (Ni and Al). In particular, we investigate the formation of $\text{Ni}(\text{Si}_x\text{Ge}_{1-x-y}\text{Sn}_y)$ on the doped Sb-doped $\text{Si}_x\text{Ge}_{1-x-y}\text{Sn}_y$ layers via annealing based on material characterization and measurements of specific contact resistivities. Our results can serve as a starting point for the investigation of $\text{Si}_x\text{Ge}_{1-x-y}\text{Sn}_y$ layers with high Si and Sn content as cladding material in optoelectronic devices such as lasers and light emitting diodes.

Keywords: SiGeSn, Sb doping SiGeSn, $\text{Ni}(\text{SiGeSn})$, annealing, Ni, Sn

(Some figures may appear in colour only in the online journal)

1. Introduction

In the past few years, the interest in a group IV light emitting device that can be easily integrated with Si photonics and electronics has increased. While the binary $\text{Ge}_{1-y}\text{Sn}_y$ has been shown to be a direct bandgap material for large enough Sn content, the ternary alloy $\text{Si}_x\text{Ge}_{1-x-y}\text{Sn}_y$ could also be a direct bandgap material in a certain compositional range with a lattice constant that can be adjusted more easily [1]. $\text{Si}_x\text{Ge}_{1-x-y}\text{Sn}_y$ has been proposed as barrier material in $\text{Ge}_{1-y}\text{Sn}_y/\text{Si}_x\text{Ge}_{1-x-y}\text{Sn}_y$ multi-quantum well laser structures [1] and has successfully been incorporated experimentally into $\text{Si}_x\text{Ge}_{1-x-y}\text{Sn}_y$ and $\text{Ge}_{1-y}\text{Sn}_y/\text{Si}_x\text{Ge}_{1-x-y}\text{Sn}_y$ multi-quantum well diodes [2, 3]. Furthermore, doped $\text{Si}_x\text{Ge}_{1-x-y}\text{Sn}_y$ can serve as cladding material for active $\text{Ge}_{1-y}\text{Sn}_y$ layers with lower bandgaps in optoelectronic devices such as light emitting diodes or lasers. Challenges in layer growth of the ternary alloys include accessing alloy compositions with high Si and Sn content as well as the doping of $\text{Si}_x\text{Ge}_{1-x-y}\text{Sn}_y$ structures for electro-optical device applications. While the growth of undoped bulk $\text{Si}_x\text{Ge}_{1-x-y}\text{Sn}_y$ using chemical vapor deposition (CVD) has successfully been achieved for

alloys with $x = 0.41$ and $y = 0.11$ [4], molecular beam epitaxy (MBE) can be used to grow ternary alloys with even higher Si (and Sn) content [5, 6], thus extending the accessible compositional range for the ternary alloy. Both n- and p-type doping in CVD-grown $\text{Si}_x\text{Ge}_{1-x-y}\text{Sn}_y$ layers as well as their incorporation into $\text{Ge}/\text{Si}_x\text{Ge}_{1-x-y}\text{Sn}_y$ heterojunction diodes has been shown [7–11], however, those studies were restricted to alloy compositions with high Ge content ($1-x-y \geq 0.75$).

Finally, the incorporation of doped $\text{Si}_x\text{Ge}_{1-x-y}\text{Sn}_y$ into optoelectronic devices requires contacts with low specific contact resistivities to minimize ohmic losses. As with the binary alloys $\text{Si}_x\text{Ge}_{1-x}$ and $\text{Ge}_{1-y}\text{Sn}_y$, the deposition of Ni onto $\text{Si}_x\text{Ge}_{1-x-y}\text{Sn}_y$ followed by annealing for stano-silicon-germanidation has been shown to lead to the formation of $\text{Ni}(\text{Si}_x\text{Ge}_{1-x-y}\text{Sn}_y)$ with potentially low specific contact resistivities [12], however, alloys with Ge content < 0.79 have not yet been investigated.

In this work, we present results on the characterization of $\text{Si}_x\text{Ge}_{1-x-y}\text{Sn}_y$ pin diodes with different alloy compositions and a Sb-doped $\text{Si}_x\text{Ge}_{1-x-y}\text{Sn}_y$ top contact layer. We show details on the material characterization of the $\text{Si}_x\text{Ge}_{1-x-y}\text{Sn}_y$

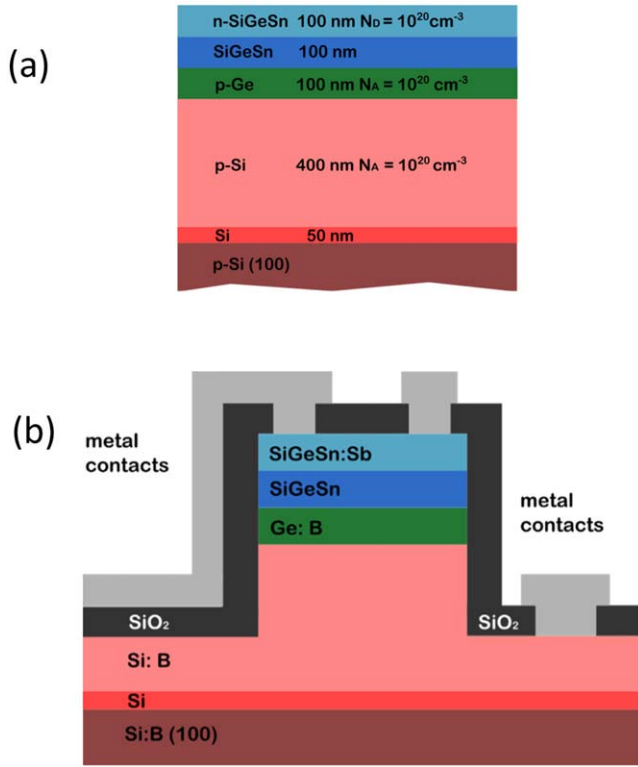


Figure 1. Schematic cross section of (a) the MBE layer structure and (b) the fabricated devices.

layers as well as on fabrication and electrical characterization of the devices. In particular, we compare Al and Ni/Al contact metallizations with respect to their specific contact resistivities and investigate the formation of Ni($\text{Si}_x\text{Ge}_{1-x-y}\text{Sn}_y$) via annealing as well as the influence of the annealing process on specific contact resistivities.

2. Fabrication and processing

All semiconductor layers were grown using solid-source MBE on 4" B-doped Si (100) substrates with a nominal resistivity of $\rho = 0.01 \, \Omega \text{ cm}$. Layer growth started with an initial 50 nm Si layer at substrate temperature $T = 600 \, ^\circ\text{C}$ to smoothen the surface and cover remaining surface contaminants. A pin heterojunction layer structure was used for all devices as shown schematically in figure 1. The p-doped region was formed by a 400 nm thick B-doped Si ($N_A = 10^{20} \text{ cm}^{-3}$) layer and a 100 nm B-doped Ge ($N_A = 10^{20} \text{ cm}^{-3}$) layer. The B-doped Ge layer was deposited at a substrate temperature $T = 330 \, ^\circ\text{C}$. Subsequent annealing starts with a temperature ramp up to a substrate temperature of $\sim 850 \, ^\circ\text{C}$ and is held for 300 s to create a virtual substrate (VS).

The high temperature serves to decrease the threading dislocation defects caused by the lattice mismatch between Si and Ge. Afterwards, a 100 nm thick intrinsic $\text{Si}_x\text{Ge}_{1-x-y}\text{Sn}_y$ layer was deposited, followed by an additional Sb-doped $\text{Si}_x\text{Ge}_{1-x-y}\text{Sn}_y$ layer (with nominal doping concentration $N_D = 10^{20} \text{ cm}^{-3}$) to form the n-contact. Three different alloy compositions were selected and chosen to approximately

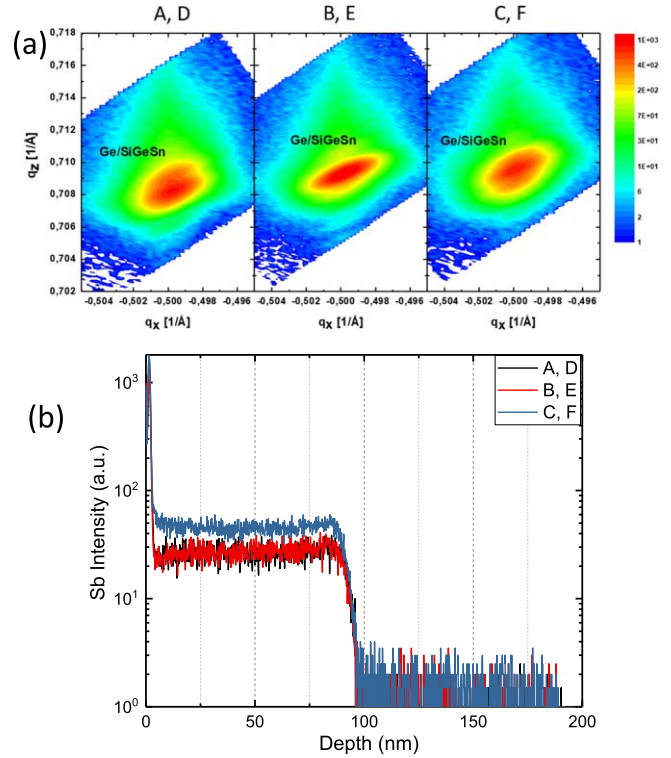


Figure 2. (a) RSM around the (-2-24) Bragg reflection for the three alloy compositions, see table 1 and (b) SIMS of nominal Sb concentration profile in the three alloys.

Table 1. $\text{Si}_x\text{Ge}_{1-x-y}\text{Sn}_y$ alloy compositions extracted from RBS [13].

Samples	Si (%)	Ge (%)	Sn (%)
A, D	26.5	66.0	7.5
B, E	37.5	53.0	9.5
C, F	46.1	41.5	12.4

match the lattice constant of the underlying Ge. Material composition and strain were investigated using x-ray diffraction (XRD) and Rutherford backscattering spectroscopy (RBS) [13]. RBS measurement results are reported in table 1.

Figure 2 shows the reciprocal space maps around the (-2-24) Bragg reflection for the three alloy compositions. The lattice matching to the underlying Ge-VS can be seen to be almost perfect for samples B, E as the Ge and the $\text{Si}_x\text{Ge}_{1-x-y}\text{Sn}_y$ peaks coincide. For all other samples two overlapping peaks are visible, indicating that the $\text{Si}_x\text{Ge}_{1-x-y}\text{Sn}_y$ layers are pseudomorphic on Ge and that lattice matching is good, i.e. strain in the $\text{Si}_x\text{Ge}_{1-x-y}\text{Sn}_y$ layers is negligible.

In order to investigate the dopant distribution in the Sb-doped $\text{Si}_x\text{Ge}_{1-x-y}\text{Sn}_y$ layer, secondary-ion mass spectroscopy was performed (figure 2(b)). The results show that the Sb doping profile is homogeneous for the first $\sim 85 \text{ nm}$ in the n-doped $\text{Si}_x\text{Ge}_{1-x-y}\text{Sn}_y$ layer and that the dopant concentration is comparable in all samples.

The MBE layers were processed into single mesa diodes. A SiO_2 hardmask defined by optical lithography with AZ

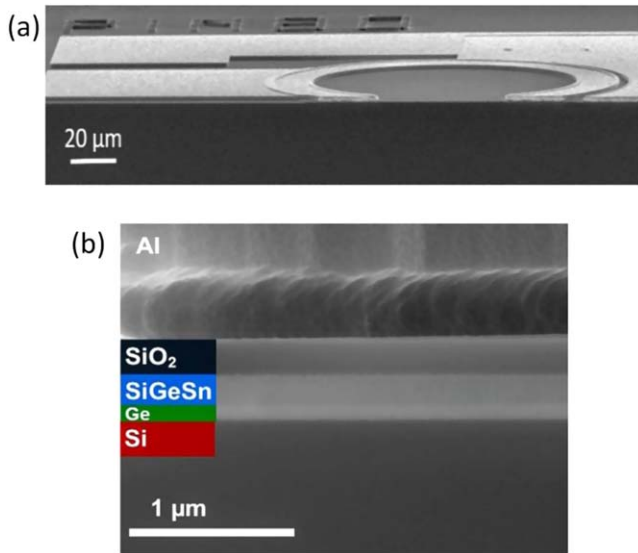


Figure 3. SEM images of a diode with (a) tilted view of a diode with a mesa radius $r = 80 \mu\text{m}$ and (b) cross sectional image of the diode layers.

Table 2. Overview of the samples with two contact metallization.

Samples	Contact metal	Special treatment
A, B, C	1.4 μm Al	None
D, E, F	30/470 nm Ni/Al	None

5214 resist and reactive ion etching was used to pattern the surface with circular mesas. An inductively coupled plasma (ICP) dry etching step using Cl_2/HBr was used to structure the mesa with heights between 358 and 406 nm. The devices were cleaned from photoresist by O_2 plasma, the oxide was removed with a 60 s BHF dip. Additional cleaning steps were used to prepare the surface for the deposition of the passivation layer. A 260 nm thick SiO_2 layer was deposited at a substrate temperature $T = 250^\circ\text{C}$ by plasma enhanced chemical vapor deposition (PECVD) to passivate the semiconductor surface. A second optical lithography step with AZ 5214 resist followed by a dry etching step with CHF_3 plasma was used to define and open contact windows. To investigate the difference in contact metallization two materials were chosen, see table 2.

On one half of the samples (samples A–C) 1.4 μm Al was sputtered to form the metal contact. Optical lithography, ICP dry etching and a H_3PO_4 wet etching step to remove any additional metal were used to structure the metal contacts. The contact pads of the other half of the samples (samples D–F) were defined through optical lithography. A HF dip was used to clean the surface prior to the deposition of 30 nm Ni and 470 nm Al by e-beam evaporation followed by a lift-off step. A schematic cross section of the fabricated pin diodes is shown in figure 1(b). The radii of the circular mesas vary between 1.5 and 80 μm . Figure 3(a) shows a scanning electron microscope (SEM) image of a tilted diode with a mesa

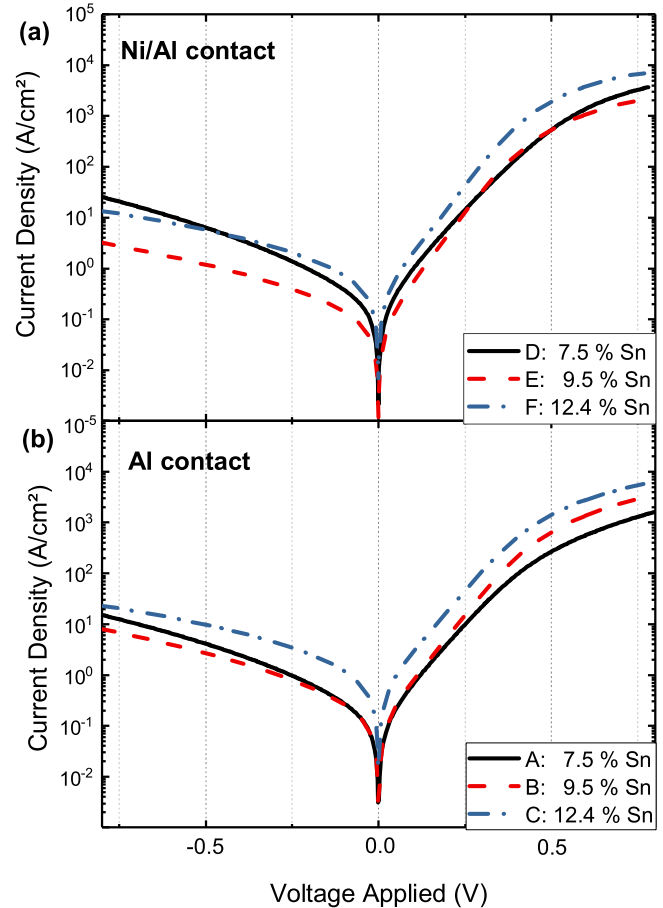


Figure 4. J - V characteristic of pin-diodes with different alloy compositions of $\text{Si}_x\text{Ge}_{1-x-y}\text{Sn}_y$ with (a) 30/470 nm Ni/Al metal contacts and (b) 1.4 μm Al metal contacts.

radius of $r = 80 \mu\text{m}$. The top metal contact pad and the surrounding bottom metal pad are visible. A cross section of the same diode is shown in figure 3(b). The different MBE layers are clearly visible. In the SEM image the difference between the Ge and the $\text{Si}_x\text{Ge}_{1-x-y}\text{Sn}_y$ layer can be observed.

3. Results and discussion

3.1. Electrical characterization

The devices were characterized electrically using a Keithley 4200 semiconductor analyzer. The current density–voltage characteristics (J - V curves) for representative diodes with identical diameters are shown in figure 4 for samples D–F with Ni/Al contacts (figure 4(a)) and for samples A–C with Al contacts (figure 4(b)). All samples show diode behavior, indicating that the MBE-based doping by Sb co-evaporation to obtain n-doped $\text{Si}_x\text{Ge}_{1-x-y}\text{Sn}_y$ layers was successful. Comparing the averaged current density at -0.8 V (figure 5) for all measured devices it can be seen that the dark current density is lowest for samples B and E with a Sn content of $\sim 9.5\%$.

This could be a result of the fact that the lattice matching conditions for the $\text{Si}_x\text{Ge}_{1-x-y}\text{Sn}_y$ layer to the underlying Ge

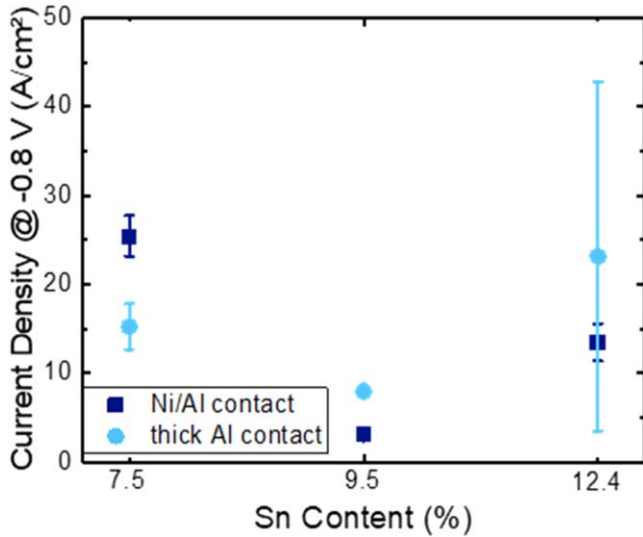


Figure 5. Comparison of current densities at $U = -0.8$ V for all diodes.

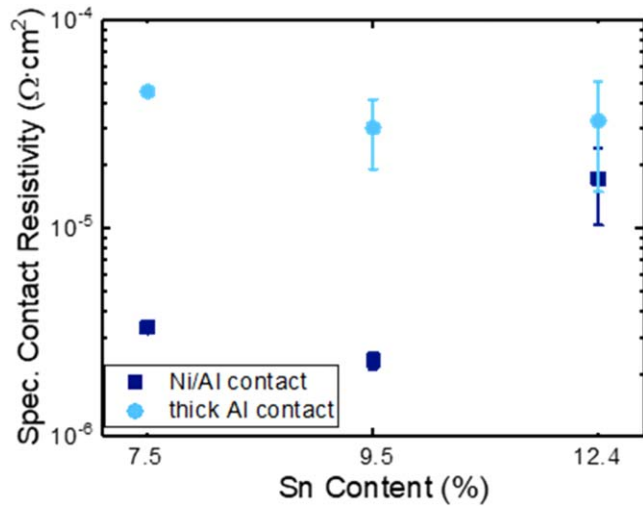


Figure 6. Comparison of the specific contact resistivities of the two metal contacts extracted from TLM.

has been met most closely for samples B and E. A transmission line model (TLM) is used to investigate specific contact resistivities of the different metallic contacts. Linear TLM structures were measured and the resulting data was fitted using the expression [14]

$$R(l) = 2 \cdot R_C + \frac{R_{sh}}{L} \cdot l. \quad (1)$$

Here, R_C is the contact resistance, R_{sh} is the semiconductor sheet resistance, L is the length of the contact (204 μm) and l is the distance between adjacent contact pads. The specific contact resistivity for each sample can then be obtained using equation (2) with the values for R_C , R_{sh} obtained from data fitting and the contact length $L = 204 \mu\text{m}$ (with transfer length L_T):

$$\rho_C = \frac{(R_C \cdot L)^2}{R_{sh}} = L_T^2 \cdot R_{sh}. \quad (2)$$

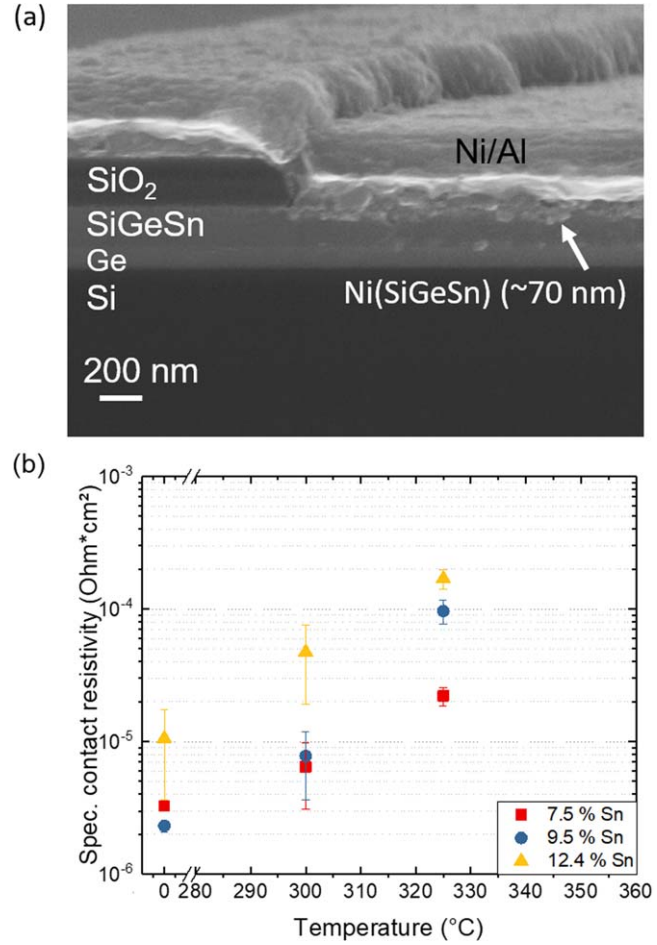


Figure 7. (a) SEM image of a diode cross section with Ni/Al contacts, passivation oxide and MBE layer structure after annealing with $T = 325$ °C and $t = 30$ s. (b) Specific contact resistivity as function of the annealing temperature for the different alloy compositions.

Figure 6 shows the dependence of the specific contact resistivity on the Sn content in the $\text{Si}_x\text{Ge}_{1-x-y}\text{Sn}_y$ layers for the different metallic contacts. The Al metal contacts exhibit an average specific resistivity of $4.5 \times 10^{-5} \text{ Ohm cm}^2$ (7.5% Sn) and $3.0 \times 10^{-5} \text{ Ohm cm}^2$ (9.5% Sn). For the Ni/Al contact an average specific contact resistivity of $3.3 \times 10^{-6} \text{ Ohm cm}^2$ (7.5% Sn) and $2.3 \times 10^{-6} \text{ Ohm cm}^2$ (9.5% Sn) could be extracted. These values are consistently lower than for the Al contacts. For 12.4% Sn the difference between the two contact materials is negligible according to the extracted specific contact resistivities.

3.2. Annealing investigations

While Ni/Al contacts clearly show lower specific contact resistivities than the Al contacts, we expect the contacts to improve further upon annealing. Previous investigations have shown that the deposition of Ni onto $\text{Si}_x\text{Ge}_{1-x-y}\text{Sn}_y$ followed by annealing leads to the formation of $\text{Ni}(\text{Si}_x\text{Ge}_{1-x-y}\text{Sn}_y)$ with potentially low specific contact resistivities [12]. Here, we subjected all samples with Ni/Al contacts to annealing steps in order to investigate the influence on specific contact resistivities.

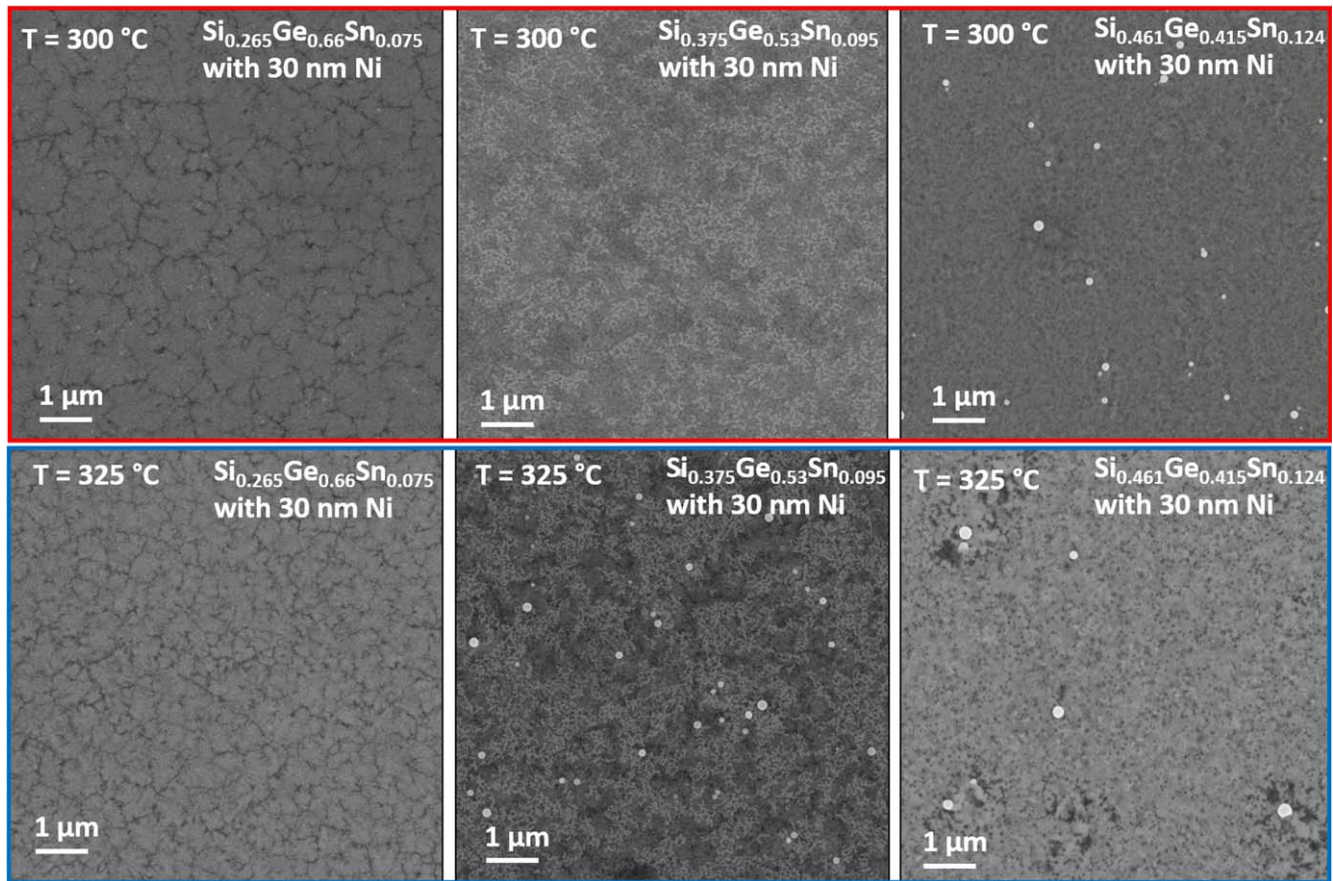


Figure 8. SEM images of samples covered with 30 nm Ni after annealing at $T = 300\text{ }^{\circ}\text{C}$ (top) and $T = 325\text{ }^{\circ}\text{C}$ (bottom) for 30 s in a N_2 ambient.

Samples D–F (see table 2) with 30 nm Ni and 470 nm Al were annealed for 30 s in N_2 at two different substrate temperatures ($300\text{ }^{\circ}\text{C}$ and $325\text{ }^{\circ}\text{C}$). The impact of the annealing steps was investigated quantitatively again based on TLM results. Qualitatively, however, the annealing step can be seen to lead to the formation of a phase containing Ni in the top $\text{Si}_x\text{Ge}_{1-x-y}\text{Sn}_y$ layer in cross sectional SEM images of the diodes after annealing: an additional layer with a thickness of approximately 70 nm can be observed after annealing with $T = 325\text{ }^{\circ}\text{C}$ and $t = 30\text{ s}$ (figure 7(a)) compared to figure 3(b). We confirm the existence of a phase containing Ni in the top $\text{Si}_x\text{Ge}_{1-x-y}\text{Sn}_y$ layer with XRD measurements that will be discussed in the following subsection.

Figure 7(b) shows the specific contact resistivity as a function of temperature for various Sn contents. Surprisingly, the specific contact resistivity can be seen to increase with increasing annealing temperature. As shown in figure 2(b) the Sb doping concentration in the n-doped $\text{Si}_x\text{Ge}_{1-x-y}\text{Sn}_y$ layer is homogenous with a layer thickness of $\sim 85\text{ nm}$. This thickness, however, is comparable to the thickness of the Ni-rich contact layer within the n-doped $\text{Si}_x\text{Ge}_{1-x-y}\text{Sn}_y$ ($\sim 70\text{ nm}$). As a result, we cannot discount the possibility that the Ni-rich contact layer effectively contacts the intrinsic $\text{Si}_x\text{Ge}_{1-x-y}\text{Sn}_y$ layer, which could explain an increased specific contact resistivity. Using a

thicker Sb doped $\text{Si}_x\text{Ge}_{1-x-y}\text{Sn}_y$ layer ($\sim 200\text{ nm}$) in future sample growth could solve this issue.

Another explanation for the increase in specific contact resistivity with increasing annealing temperature could be the formation of $\text{Ni}_5(\text{Si}_x\text{Ge}_{1-x-y}\text{Sn}_y)_3$ rather than $\text{Ni}(\text{Si}_x\text{Ge}_{1-x-y}\text{Sn}_y)$ during annealing and a resulting increase in specific contact resistivity. Therefore, we also performed an XRD analysis, which will be discussed in the next subsection.

3.3. $\text{Ni}(\text{Si}_x\text{Ge}_{1-x-y}\text{Sn}_y)$ alloy formation

Additional experiments were performed in order to investigate the $\text{Ni}(\text{Si}_x\text{Ge}_{1-x-y}\text{Sn}_y)$ contact formation in our layers. To carry out these experiments, additional samples were fabricated based on $\text{Si}_x\text{Ge}_{1-x-y}\text{Sn}_y$ with the three different concentrations reported in table 1. Here, the samples were covered with unstructured Ni layers with a thickness of 30 nm and then subjected to different annealing steps. The surface morphology was investigated in the SEM and XRD measurements were used to investigate whether $\text{Ni}_5(\text{Si}_x\text{Ge}_{1-x-y}\text{Sn}_y)_3$ or $\text{Ni}(\text{Si}_x\text{Ge}_{1-x-y}\text{Sn}_y)$ was formed. In figure 8, SEM images show the surfaces of the different samples after annealing steps at $T = 300\text{ }^{\circ}\text{C}$ and $T = 325\text{ }^{\circ}\text{C}$ in N_2 for 30 s. While no clear surface changes can be observed in the $\text{Si}_{0.265}\text{Ge}_{0.66}\text{Sn}_{0.075}$ sample as the annealing temperature is increased from $T = 300\text{ }^{\circ}\text{C}$ to $T = 325\text{ }^{\circ}\text{C}$, the same increase

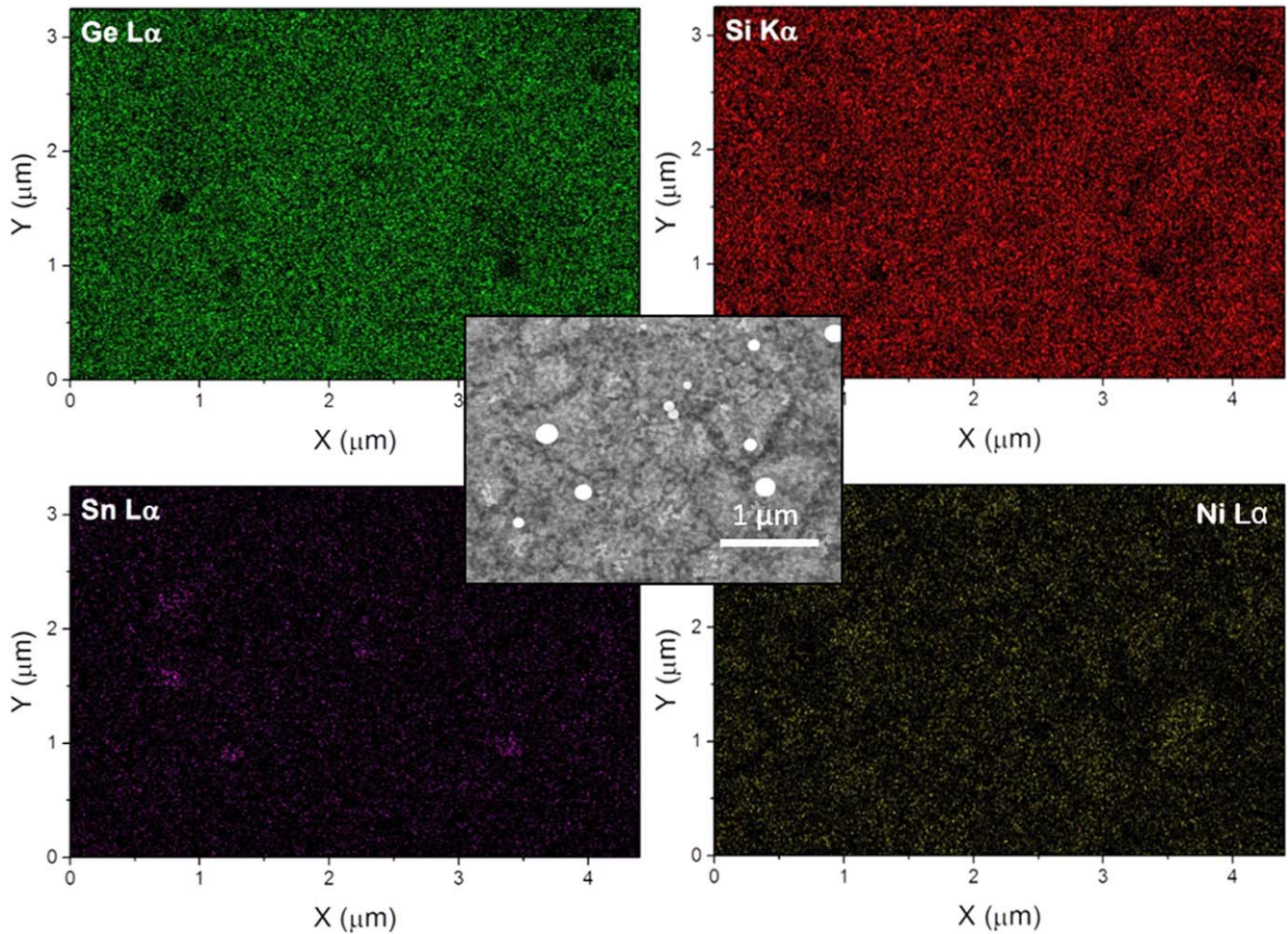


Figure 9. EDX analysis for the materials Ge, Si, Sn and Ni on the surface of sample $\text{Si}_{0.375}\text{Ge}_{0.53}\text{Sn}_{0.095}$ with 30 nm Ni after annealing at $T = 325^\circ\text{C}$ for 30 s in a N_2 ambient. The inset shows a SEM image of this region on the surface.

can be seen to lead to the formation of droplets on the $\text{Si}_{0.375}\text{Ge}_{0.53}\text{Sn}_{0.095}$ sample surface for the sample with higher Sn content. The $\text{Si}_{0.461}\text{Ge}_{0.415}\text{Sn}_{0.124}$ sample with the highest Sn content shows droplets on its surface for both annealing temperatures. Further investigations using energy-dispersive x-ray spectroscopy (EDX) were carried out to determine the material composition of the droplets. Figure 9 presents the results of the EDX analysis for the elements Ge, Si, Sn and Ni on the sample surface of the $\text{Si}_{0.375}\text{Ge}_{0.53}\text{Sn}_{0.095}$ sample. Ge and Si are distributed nearly homogeneously on the sample surface except for some places, where the signal intensity drops markedly. These positions coincide with positions with high intensity for the Sn material analysis (colored purple) as well as with the positions of the precipitates seen in the SEM inset. Therefore, the droplet formation is as a result of Sn precipitation as Ni is incorporated

Finally, figure 10 presents the 2 theta scans obtained through XRD to investigate the phase formation of $\text{Ni}(\text{Si}_x\text{Ge}_{1-x-y}\text{Sn}_y)$ for annealing temperatures $T = 300^\circ\text{C}$ and $T = 325^\circ\text{C}$. Peaks around 45° are observed for all samples at all annealing temperatures. We attribute these to

the formation of the mono- $\text{Ni}(\text{Si}_x\text{Ge}_{1-x-y}\text{Sn}_y)$ phase for all samples and annealing temperatures [12]. We also investigated the effect of annealing on the semiconductor layers underneath the $\text{Ni}(\text{Si}_x\text{Ge}_{1-x-y}\text{Sn}_y)$ contacts by rocking curves (figure 11). While annealing can be seen to reduce the intensity of the $\text{Si}_x\text{Ge}_{1-x-y}\text{Sn}_y$ peaks, which can be attributed to the fact that the formation of $\text{Ni}(\text{Si}_x\text{Ge}_{1-x-y}\text{Sn}_y)$ reduces the thickness of the $\text{Si}_x\text{Ge}_{1-x-y}\text{Sn}_y$ layers by ~ 70 nm, the peak shape remains largely unchanged. Furthermore, we do not observe the formation of additional peaks that could indicate alloy decomposition of the $\text{Si}_x\text{Ge}_{1-x-y}\text{Sn}_y$ as a result of the annealing. Based on these results we conclude that the effect of annealing on the $\text{Si}_x\text{Ge}_{1-x-y}\text{Sn}_y$ semiconductor layers below the $\text{Ni}(\text{Si}_x\text{Ge}_{1-x-y}\text{Sn}_y)$ contacts is negligible, i.e. the Sn precipitation observed in figure 8 originates mainly from the $\text{Ni}(\text{Si}_x\text{Ge}_{1-x-y}\text{Sn}_y)$ layer but not from the $\text{Si}_x\text{Ge}_{1-x-y}\text{Sn}_y$ semiconductor layers below. Future analysis based on transmission electron microscopy could be used to investigate the crystal structure and material composition of the $\text{Ni}(\text{Si}_x\text{Ge}_{1-x-y}\text{Sn}_y)$ layers in more detail.

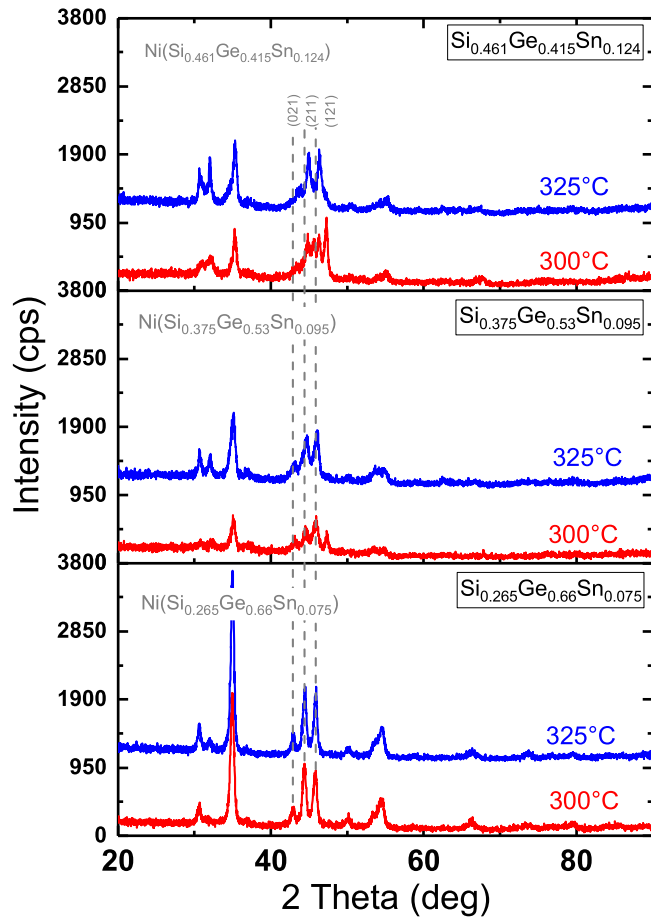


Figure 10. XRD 2 theta scans to investigate the $\text{Ni}(\text{Si}_x\text{Ge}_{1-x-y}\text{Sn}_y)$ phase formation at annealing temperatures (300 °C and 325 °C) and for the different $\text{Si}_x\text{Ge}_{1-x-y}\text{Sn}_y$ alloys.

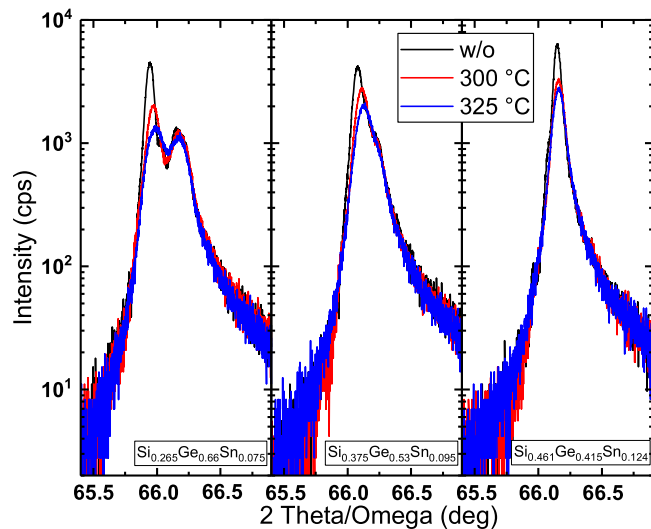


Figure 11. XRD rocking curves of the $\text{Si}_x\text{Ge}_{1-x-y}\text{Sn}_y/\text{Ge}$ peaks after annealing at $T = 300$ °C and $T = 325$ °C. While the intensity of the $\text{Si}_x\text{Ge}_{1-x-y}\text{Sn}_y$ peaks is reduced after annealing, no additional peaks form, i.e. no alloy decomposition can be observed.

4. Conclusion

$\text{Si}_x\text{Ge}_{1-x-y}\text{Sn}_y$ alloys allow to decouple the bandgap from the lattice constant for possible applications in optoelectronic devices. We demonstrated the fabrication of $\text{Si}_x\text{Ge}_{1-x-y}\text{Sn}_y$ heterojunction pin diodes with three different alloy compositions. We successfully developed a strategy to dope $\text{Si}_x\text{Ge}_{1-x-y}\text{Sn}_y$ layers with Sb to create an n-doped top contact. Investigations regarding the metallization with Al and Ni/Al as contact material showed that the use of Ni/Al results in a specific contact resistivity of $\sim 2.3 \times 10^{-6} \text{ Ohm cm}^2$ ($\text{Si}_{0.375}\text{Ge}_{0.53}\text{Sn}_{0.095}$) and $3.3 \times 10^{-6} \text{ Ohm cm}^2$ ($\text{Si}_{0.265}\text{Ge}_{0.66}\text{Sn}_{0.075}$). Those specific contact resistivities were roughly one order of magnitude lower than for devices with Al metal contacts. Annealing investigations were carried out to investigate the formation of $\text{Ni}(\text{Si}_x\text{Ge}_{1-x-y}\text{Sn}_y)$ contact layers. While we observe an increase in specific contact resistivity rather than a decrease for increasing annealing temperatures, we attribute this to the fact that the $\text{Ni}(\text{Si}_x\text{Ge}_{1-x-y}\text{Sn}_y)$ contact layers extend into the intrinsic $\text{Si}_x\text{Ge}_{1-x-y}\text{Sn}_y$ layers of our samples. A thicker Sb doped $\text{Si}_x\text{Ge}_{1-x-y}\text{Sn}_y$ layer used for contact formation in future experiments could solve this issue.

Furthermore, we investigated the formation of $\text{Ni}(\text{Si}_x\text{Ge}_{1-x-y}\text{Sn}_y)$ through annealing based on EDX analysis and XRD measurements for all samples and found that, depending on the annealing temperature, the formation of $\text{Ni}(\text{Si}_x\text{Ge}_{1-x-y}\text{Sn}_y)$ can lead to Sn precipitation and the formation of Sn droplets on the sample surface especially for samples with high Si and high Sn content. Optimal annealing temperatures for such alloys have to be investigated further in order to determine processing parameters that enable the reliable formation of contacts to n-doped $\text{Si}_x\text{Ge}_{1-x-y}\text{Sn}_y$ alloys with low specific contact resistivities. Other investigations [15] showed that the incorporation of for example Al reduces the diffusion of Ni and can stabilize the reactions of Ni–Si and Ni–Ge.

Our results can form the basis for the fabrication of $\text{Si}_x\text{Ge}_{1-x-y}\text{Sn}_y$ layers with high Si and Sn content as cladding material for $\text{Si}_x\text{Ge}_{1-x-y}\text{Sn}_y$ and $\text{Ge}_{1-y}\text{Sn}_y$ based optoelectronic devices.

Acknowledgments

This research received funding by the Deutsche Forschungsgemeinschaft (DFG) (OE 520/7-1, FI 1511/4-1).

ORCID iDs

Caterina J Clausen <https://orcid.org/0000-0002-8950-5990>

Florian Baerwolf <https://orcid.org/0000-0002-3640-9700>

References

- [1] Chang G-E, Chang S-W and Chuang S-L 2010 Strain-balanced multiple-quantum-well lasers *IEEE J. Quantum Electron.* **46** 1813–20
- [2] Fischer I A *et al* 2015 Growth and characterization of SiGeSn quantum well photodiodes *Opt. Express* **23** 25048
- [3] Stange D *et al* 2017 Short-wave infrared LEDs from GeSn/SiGeSn multiple quantum wells *Optica* **4** 185–8
- [4] D'Costa V R, Fang Y-Y, Tolle J, Kouvetakis J and Menéndez J 2009 Tunable optical gap at a fixed lattice constant in group-IV semiconductor alloys *Phys. Rev. Lett.* **102** 107403
- [5] Wendav T *et al* 2016 Compositional dependence of the band-gap of $\text{Ge}_{1-x-y}\text{Si}_x\text{Sn}_y$ alloys *Appl. Phys. Lett.* **108** 242104
- [6] Yamaha T, Shibayama S, Asano T, Kato K, Sakashita M, Takeuchi W, Nakatsuka O and Zaima S 2016 Experimental observation of type-I energy band alignment in lattice-matched $\text{Ge}_{1-x-y}\text{Si}_x\text{Sn}_y/\text{Ge}$ heterostructures *Appl. Phys. Lett.* **108** 061909
- [7] Beeler R T, Smith D J, Kouvetakis J and Menéndez J 2012 GeSiSn photodiodes with 1 eV optical gaps grown on Si(100) and Ge(100) platforms *IEEE J. Photovolt.* **2** 434–40
- [8] Beeler R T, Xu C, Smith D J, Grzybowski G, Menéndez J and Kouvetakis J 2012 Compositional dependence of the absorption edge and dark currents in $\text{Ge}_{1-x-y}\text{Si}_x\text{Sn}_y/\text{Ge}(100)$ photodetectors grown via ultra-low-temperature epitaxy of Ge_4H_{10} , Si_4H_{10} , and SnD_4 *Appl. Phys. Lett.* **101** 221111
- [9] Xu C, Beeler R T, Grzybowski G J, Chizmeshya A V G, Smith D J, Menéndez J and Kouvetakis J 2012 Molecular synthesis of high-performance near-IR photodetectors with independently tunable structural and optical properties based on Si–Ge–Sn *J. Am. Chem. Soc.* **134** 20756–67
- [10] Xu C, Beeler R T, Jiang L, Gallagher J D, Favaro R, Menéndez J and Kouvetakis J 2014 Synthesis and optical properties of Sn-rich $\text{Ge}_{1-x-y}\text{Si}_x\text{Sn}_y$ materials and devices *Thin Solid Films* **557** 177–82
- [11] Gallagher J D, Xu C, Senaratne C L, Aoki T, Wallace P M, Kouvetakis J and Menéndez J 2015 $\text{Ge}_{1-x-y}\text{Si}_x\text{Sn}_y$ light emitting diodes on silicon for mid-infrared photonic applications *J. Appl. Phys.* **118** 135701
- [12] Wirths S, Troitsch R, Mussler G, Hartmann J-M, Zaumseil P, Schroeder T, Mantl S and Buca D 2015 Ternary and quaternary Ni(Si)Ge(Sn) contact formation for highly strained Ge p- and n-MOSFETs *Semicond. Sci. Technol.* **30** 055003
- [13] Fischer I A, Berrier A, Hornung F, Oehme M, Zaumseil P, Capellini G, Driesch N, von den, Buca D and Schulze J 2017 Optical critical points of $\text{Si}_x\text{Ge}_{1-x-y}\text{Sn}_y$ alloys with high Si content *Semicond. Sci. Technol.* **32** 124004
- [14] Sze S M and Ng K K 2007 *Physics of Semiconductor Devices* 3rd edn (New York: Wiley)
- [15] Zhang B *et al* 2011 Epitaxial growth of $\text{Ni}(\text{Al})\text{Si}_{0.7}\text{Ge}_{0.3}$ on $\text{Si}_{0.7}\text{Ge}_{0.3}/\text{Si}(100)$ by Al interlayer mediated epitaxy *Appl. Phys. Lett.* **98** 252101